AGU PUBLICATIONS

JGR

Journal of Geophysical Research: Space Physics

RESEARCH ARTICLE
10.1002/2014JA020172

Key Points:
- Model IB latitude lower for higher-energy ions and under higher *Kp* or Pd
- Good agreement between the model IB and THEMIS and FAST observations
- Current sheet scattering is the main cause of energy-dependent IB

Correspondence to:
C. Yue,
yuechao@atmos.ucla.edu

Citation:
Yue, C., C.-P. Wang, L. Lyons, J. Liang, E. F. Donovan, S. G. Zaharia, and M. Henderson (2014), Current sheet scattering and ion isotropic boundary under 3-D empirical force-balanced magnetic field, *J. Geophys. Res. Space Physics*, *119*, 8202–8211, doi:10.1002/2014JA020172.

Received 12 MAY 2014
Accepted 11 SEP 2014
Accepted article online 18 SEP 2014
Published online 16 OCT 2014

Current sheet scattering and ion isotropic boundary under 3-D empirical force-balanced magnetic field

Chao Yue[1], Chih-Ping Wang[1], Larry Lyons[1], Jun Liang[2], Eric F. Donovan[2], Sorin G. Zaharia[3], and Michael Henderson[3]

[1]Department of Atmospheric and Oceanic Sciences, University of California, Los Angeles, California, USA, [2]Department of Physics and Astronomy, University of Calgary, Calgary, Alberta, Canada, [3]Space Science and Applications, Los Alamos National Laboratory, Los Alamos, New Mexico, USA

Abstract To determine statistically the extent to which current sheet scattering is sufficient to account for the observed ion isotropic boundaries (IBs) for <30 keV ions, we have computed IBs from our 3-D empirical force-balanced magnetic field, identified IBs in FAST observations, and investigated the model-observation consistency. We have found in both model and FAST results the same dependences of IB latitudes on magnetic local time, ion energy, *Kp*, and solar wind dynamic pressure (P_{SW}) levels: IB moves to higher latitudes from midnight toward dawn/dusk and to lower latitudes as energy increases and as *Kp* or P_{SW} increases. The model predicts well the observed energy dependence, and the modeled IB latitudes match fairly well with those from FAST for $Kp = 0$. As *Kp* increases, the latitude agreement at midnight remains good but a larger discrepancy is found near dusk. The modeled IBs at the equator are located around the earthward boundary of highly isotropic ions observed by Time History of Events and Macroscale Interactions during Substorms at midnight and postmidnight, but with some discrepancy near dusk under high *Kp*. Thus, our results indicate that current sheet scattering generally plays the dominant role. The discrepancies suggest the importance of pitch angle scattering by electromagnetic ion cyclotron waves, which occur more often from dusk to noon and are more active during higher *Kp*. The comparison with the observed IBs is better with our model than under the nonforce-balanced T89, indicating that using a forced-balanced model improves the description of the magnetic field configuration and reinforces our conclusions regarding the role of current sheet scattering.

1. Introduction

The stretched magnetic field configuration in the presence of a current sheet in the nightside part of the magnetosphere leads to pitch angle scattering of particles due to violation of the first adiabatic invariant. When field lines become stretched and the corresponding magnetic field curvature radius Rc and the gyroradius ρ become comparable, particles undergo nonadiabatic pitch angle scattering, resulting in isotropic pitch angle distribution and filling of the loss cone. Based on previous studies [*Sergeev and Tsyganenko*, 1982; *Sergeev et al*., 1983; *Sergeev and Malkov*, 1988; *Sergeev and Gvozdevsky*, 1995], the pitch angle scattering due to the current sheet becomes effective when the ratio of Rc to ρ is lower than ~8. The current sheet scattering is energy dependent because of its ρ dependence. It is capable of scattering plasma sheet ions of thermal energy (> 1 keV), consistent with their observed isotropic populations [*Wang et al*., 2012]. By using the Tsyganenko-01 model, *Lvova et al*. [2005] showed that the protons with energies of ~80 keV the transition between adiabatic and nonadiabatic behaviors on the nightside occurs at $5 - 9\ R_E$ at the equator under different solar wind conditions.

Current sheet scattering has been considered as a major cause of the isotropic boundary (IB) observed in the tail and at low altitudes, this boundary separating pitch angle distributions with an empty loss cone from those with a full loss cone. As a low-altitude satellite moves poleward, it encounters first the IB at auroral latitudes and then the polar cap boundary. The IB corresponds to the earthward edges of isotropic protons at the equator. It has been shown observationally that the latitude of the IB is a function of magnetic local time (MLT), particle energy, and the state of the magnetosphere. The ion IB and the equatorward boundary of the associated proton aurora are statistically located at higher magnetic latitudes at dusk and dawn than at midnight [*Donovan et al*., 2003a; *Lvova et al*., 2005]. The IBs are located at lower latitudes for higher-energy ions [*Newell et al*., 1998; *Shevchenko et al*., 2010] and under stronger geomagnetic activities [*Lvova et al*., 2005].

In addition to current sheet scattering, wave-particle interaction can also cause pitch angle scattering and filling of the loss cone. In the inner magnetosphere, electromagnetic ion cyclotron (EMIC) waves can sufficiently scatter ions above 1 keV [*Jordanova et al*., 2001].

Past studies have provided evidence for the role of current sheet scattering in controlling the IB latitudes. For example, *Sergeev et al*. [1993] showed that the IB for 100 keV protons at various local times has a very high correlation (~0.9) with the inclination of the *B* field as measured on the nightside at geosynchronous orbit, indicating that the IB latitude is effectively controlled by the tail magnetic field. By using the Tsyganenko-01 model, *Ganushkina et al*. [2005] computed IB locations and compared them with the statistical distributions of the 31–80 keV proton IB measured by the Polar satellite at midaltitudes and those observed by NOAA satellites at low altitudes. They concluded that pitch angle scattering by the tail current sheet is the basic mechanism controlling the transition from isotropic to anisotropic distributions in the near-equatorial region. *Shevchenko et al*. [2010] investigated mapping accuracy in the T96, AM-01, and AM-02 models by comparing hundreds of 80 keV proton IB observations from NOAA with the model-predicted IBs due to tail current sheet scattering. Their results indicate that a field model that can more accurately reproduce the observed magnetic field in the current sheet predicts better the IB latitudes. However, the above observational studies and comparisons with models focused mainly on high-energy ions (>30 keV). For ions of the typical plasma sheet thermal energy (1 to 30 keV), the IB latitudes and the role of current sheet scattering remain to be determined from observations and models.

In the above investigations of the role of current sheet scattering in controlling IBs, empirical magnetic field models were used. However, these empirical magnetic field models are not in force balance with observed plasma pressures and can overestimate or underestimate the magnetic fields in different regions [*McCollough et al*., 2008]. The *Shevchenko et al*. [2010] study has pointed out the importance of using more accurate magnetic field model in predicting IB. Recently, we have developed an empirical modeling approach to obtain 3-D force-balanced magnetic field configurations in the near-Earth magnetosphere inside 30 R_E [*Wang et al*., 2013; *Yue et al*., 2013] that is entirely different from other empirical magnetic field modeling, such as the Tsyganenko models. Other empirical models were built by fitting the model magnetic field from a framework of postulated currents to observed magnetic field. Our model magnetic field, on the other hand, is solved from the force balance equation with observed equatorial plasma pressure. Since the model is not based on the observed magnetic field, we used magnetic field data for validation and found fairly good agreement over wide ranges of *Kp* and P_{SW} [*Wang et al*., 2013]. Since our model is in force balance and shows good agreement with magnetic field observations, it should provide better estimates of current scattering and the associated IB than do other empirical magnetic field models.

In this study, we estimate the current sheet scattering of 1–30 keV ions using our force-balanced magnetic field, identify the equatorial IB from the Time History of Events and Macroscale Interactions during Substorms (THEMIS) observations and low-altitude IB from the FAST measurements, and determine the role of current sheet scattering through the model-observation comparison. In section 2, we briefly describe the force-balanced magnetic field modeling and the FAST measurements. The model-predicted IBs, as well as the THEMIS and FAST IBs, for different energies and *Kp* and P_{SW} levels and their comparisons are presented in section 3. The differences from the predictions of the *Kp*-dependent Tsyganenko 87 (T89) model are discussed in section 4. Section 5 summarizes our main findings.

2. Model and Observation

2.1. Computing 3-D Empirical Force-Balanced Magnetic Field and Current Sheet Scattering Parameters

Here we briefly describe the working principles of our 3-D empirical force-balanced pressure and magnetic field modeling (details of the modeling can be found in *Wang et al*. [2013] and *Yue et al*. [2013]). We first established the empirical equatorial plasma pressure based on Geotail and THEMIS data from 1996 to 2010 [*Wang et al*., 2013]. The pressure data were normalized to correspond to $P_{SW} = 1.5$ and 3 nPa using linear fitting and then sorted into different *Kp* levels (from 0 to 4). The empirical

pressure model is established by fitting the spatial pressure distributions to an analytical function with nine fitting parameters (b1 to b9) as follows:

$$P_m(r,\ \varphi)\ (\mathrm{nPa}) = e^{\mathrm{b1}\cdot r}[\mathrm{b2} + \mathrm{b3sin}(\varphi) + \mathrm{b4sin2}(\varphi)] + r^{\mathrm{b5}}[\mathrm{b6} + \mathrm{b7sin}(\varphi) + \mathrm{b8sin2}(\varphi)] + \mathrm{b9},$$

where r is the radial distance in R_E and φ is the azimuthal angle (0° at noon, 90° at dusk, 180° at midnight, and 270° at dawn). b1 to b4 mainly control the pressure in the inner magnetosphere while b5 to b9 determine the plasma sheet pressure. More details about the fitting method and the fitting parameters are available in *Wang et al.* [2013].

Using the empirical pressure distribution as an input, the magnetic field model computes the force-balanced magnetic field by solving the single-fluid force balance equation $\nabla P = J \times B$ in terms of Euler potentials as $B = \nabla\alpha \times \nabla\beta$, where P is plasma pressure given by the above empirical pressure model. The 3-D force balance equation can be decoupled into two coupled "quasi-2-D" equations in the directions parallel to $(B \times \nabla\alpha)$ and $(B \times \nabla\beta)$, respectively, as follows:

$$J\cdot\nabla\alpha = \nabla\cdot\left[(\nabla\alpha)^2\nabla\beta - (\nabla\alpha\cdot\nabla\beta)\nabla\alpha\right] = -\frac{\partial P}{\partial\beta} \quad (1)$$

$$J\cdot\nabla\beta = \nabla\cdot\left[(\nabla\beta\cdot\nabla\alpha)\nabla\beta - (\nabla\beta)^2\nabla\alpha\right] = \frac{\partial P}{\partial\alpha} \quad (2)$$

The constant α and β surfaces are found from solving equations (1) and (2) numerically through an alternating iterative process. B and the inhomogeneous terms on the right-hand sides ($\frac{\partial P}{\partial\alpha}$ and $\frac{\partial P}{\partial\beta}$) are prescribed at the model boundary with values obtained from an empirical magnetic field model (in this study the boundary values were obtained from the Tsyganenko 89 (T89) model since it is controlled by *Kp* and extends to the farther downtail region of ~30 R_E of our magnetic field model boundary).

With the computed 3-D force-balanced magnetic fields, we are able to calculate the field curvature radius Rc, the proton gyroradius ρ, and tail current sheet (TCS) scattering parameter $K = \mathrm{Rc}/\rho$ on the equatorial plane using $\mathrm{Rc} = B_Z/(\mathrm{d}Br/\mathrm{d}z)$, where B_Z is the equatorial magnetic field and Br is the radial component of the magnetic field off the equatorial plane, $\rho = mV/eB_Z$, where m is the mass, V is the velocity of the particle, and e is the electron charge. The computed equatorial locations and ionospheric latitudes of IB ($K = 8$) [*Sergeev et al.*, 1983] for different energies and their comparisons with equatorial THEMIS and low-altitude FAST observations are shown in section 3.

2.2. FAST Data for Isotropic Boundary Latitudes

The FAST satellite measures the fluxes of both trapped particles and particles within the loss cone [*Carlson et al.*, 1998], allowing determination of the IB. FAST was launched on 21 August 1996 into an elliptical orbit of 350 km by 4175 km that cross the auroral oval 4 times per orbit (approximately 11 orbits per day) over a wide range of altitudes, local times, and seasons. The plasma instrumentation (electrostatic analyzer (ESA)) includes two pairs of "top-hat" electrostatic analyzers to measure the high-resolution energy spectra of ions (3 eV–25 keV) and electrons (4 eV–30 keV) in 48 energy channels at 32 pitch angle bins every 78 ms. In this study, we have collected ~12,000 IB cases from 1996 to 2009 under different *Kp* and P_{SW} levels.

3. Results

3.1. Current Sheet Scattering in the Plasma Sheet

Figure 1 shows the radial variations of the main parameters obtained from the 3-D force-balanced magnetic field and the associated TCS scattering parameter K for $Kp = 1$, $P_{SW} = 1.5$ (Figure 1a) and for $Kp = 3$ and $P_{SW} = 3$ (Figure 1b). The first row shows the magnetic field lines along the midnight meridian originated from different ionospheric latitudes (different colors indicate different latitudes). The second row shows the equatorial magnetic field B_Z. The third row shows the Br component at $Z = 0.5\ R_E$. The last three rows show the equatorial field line curvature radius, gyroradius, and K for protons of two typical near-Earth plasma sheet energies (1 keV in blue lines and 30 keV in red lines). The solid horizontal black line in the sixth row marks

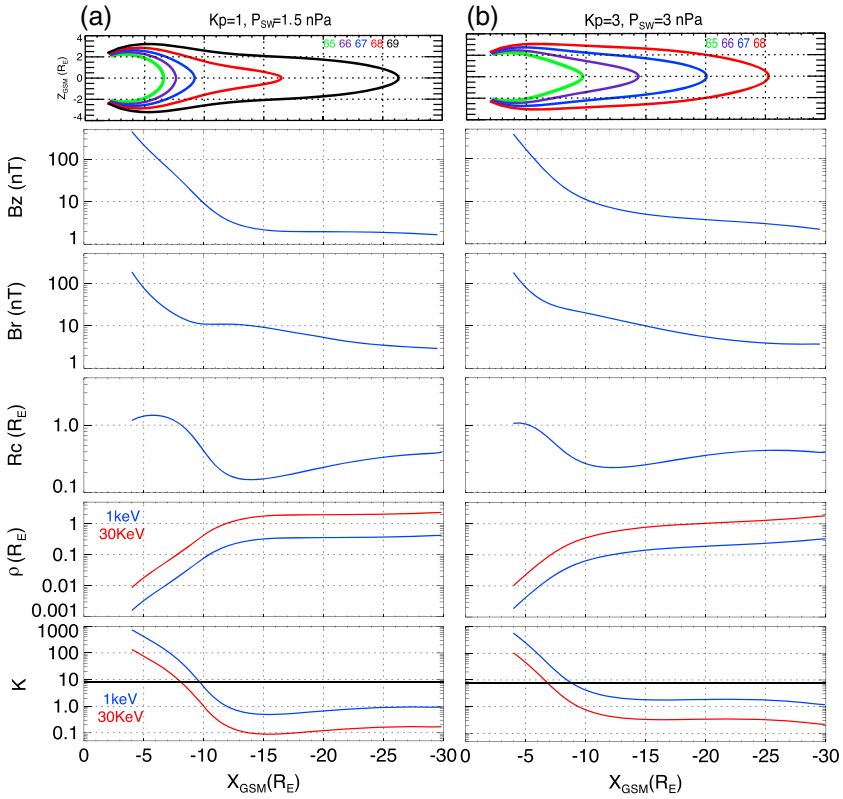

Figure 1. Midnight radial profiles of the key parameters of IB calculation for (a) $Kp = 1$ and $P_{SW} = 1.5$ nPa and (b) $Kp = 3$ and $P_{SW} = 3$ nPa cases. The first row shows the magnetic field lines of different ionospheric latitudes; the second row shows B_Z at $z = 0$; the third row shows Br at $z = 0.5\ R_E$; the fourth row shows the equatorial magnetic field curvature; and the last two rows show the equatorial gyroradius and the TCS scattering parameter K for 1 (blue curve) and 30 (red curve) keV protons.

$K = 8$. As shown in Figures 1a and 1b, B_Z decreases sharply with increasing radial distance r from dipole like to taillike. This transition region is at ~12 R_E for $Kp = 1$ and moves earthward to ~9 R_E for $Kp = 3$. Tailward of the transition region, B_Z decreases slowly with increasing r in the magnetotail. Similar radial variations are seen in Br. As discussed in *Yue et al*. [2013], the earthward motion of the transition region is a result of the magnetic field at smaller r becoming more stretched. This strengthens the magnetic force to balance the increased pressure gradient resulting from the enhanced earthward driving of the plasma sheet by stronger convection during higher Kp. The curvature radius computed from Br is about 1 R_E in the inner magnetosphere but drops sharply at ~8 (6) R_E to a minimum value of 0.15 (0.25) R_E at ~13 (11) R_E for $Kp = 1$ (3). The variation of B_Z causes the gyroradius ρ to rapidly increase outward from the Earth in the transition region and then increase gradually in the tail. For protons of the same energy, the gyroradius for $Kp = 3$ is larger in the inner magnetosphere and smaller in the tail than that for $Kp = 1$. As a result of the above radial variations of the curvature radius and the gyroradius, the K values of 30 keV protons for $Kp = 1$ is ~100 at $r \sim 5\ R_E$ and drops rapidly to 8 at $r = 8\ R_E$ and remains below 8 in the tail. This indicates that the 30 keV protons tailward of $r = 8\ R_E$ are expected to undergo pitch angle scattering and have an isotropic pitch angle distribution with a filled loss cone, while those earthward of $r = 8\ R_E$ do not. The IB for the 30 keV protons is thus located at $r = 8\ R_E$ at midnight. The IB moves earthward for the same proton energy during higher Kp or for higher energy under the same Kp.

Figure 2 illustrates the equatorial distributions of the scattering parameter K for 1 and 30 keV protons for different Kp and P_{SW} levels. It can be seen that the K values for different energy protons have similar spatial variations with K being the lowest at midnight tail and increasing toward the dawn and dusk flanks and toward the Earth. The black stars mark the IB locations where $K = 8$. The IB location is closest to the Earth at midnight and moves to larger r toward dawn and dusk due to the magnetic field being more stretched at

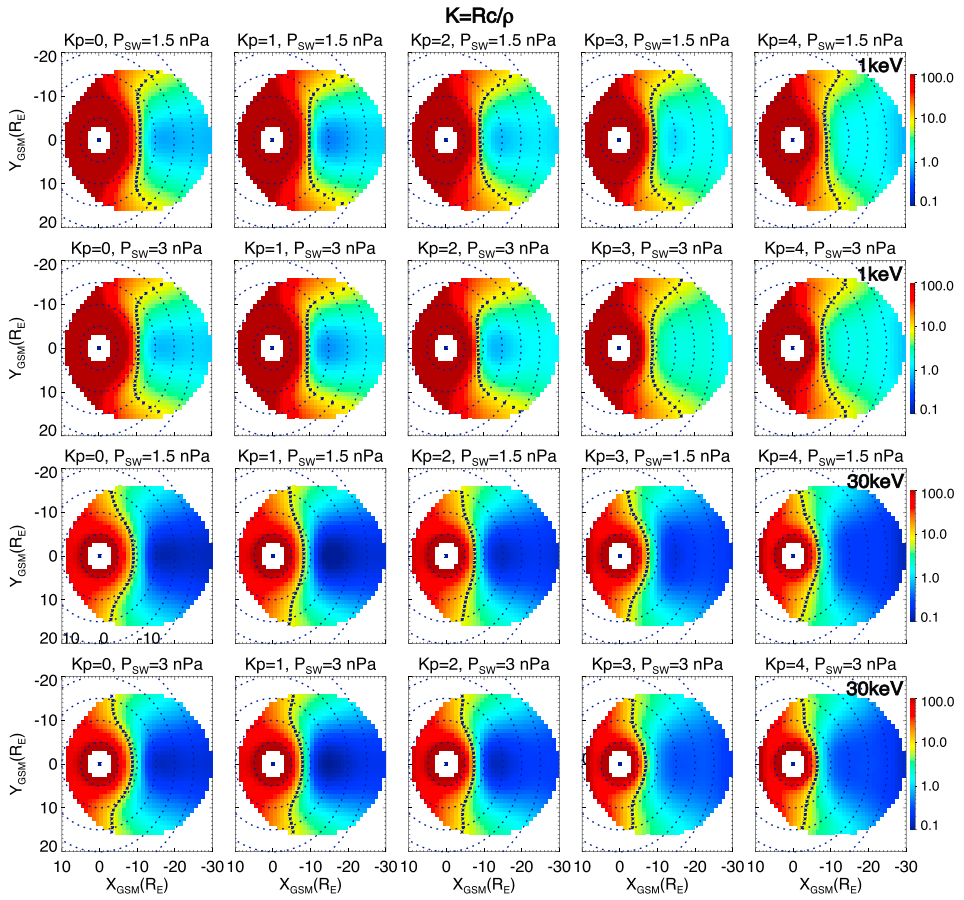

Figure 2. The TCS scattering parameter K for 1 and 30 keV protons on the equatorial plane for different Kp and P_{SW} levels. The black stars mark $K = 8$.

midnight than at dawn and dusk. The IB for the same energy at all MLTs moves earthward with increasing Kp or P_{SW}. For the same Kp and P_{SW} level, the IBs for 30 keV protons at all MLTs are a few R_E earthward of those for 1 keV protons.

Protons in the equatorial plasma sheet tailward of IB are expected to be isotropized by TCS scattering, thus becoming highly isotropic in their pitch angle distributions. We have previously investigated the pitch angle anisotropy of ions of different energies observed by THEMIS from the tail plasma sheet to the inner magnetosphere [*Wang et al.*, 2012]. The anisotropy is indicated by A,

$$A \equiv \frac{\int_0^{\pi/2} f(\alpha_0)\sin^3\alpha_0\, d\alpha_0}{\int_0^{\pi/2} f(\alpha_0)\cos^2\alpha_0 \sin\alpha_0\, d\alpha_0} - 1,$$

where f is phase space density and α_0 is pitch angle. A pitch angle distribution with $|A| < 0.1$ is considered highly isotropic. Figure 3 shows the occurrence rates of highly isotropic ions of 12.3 and 27.7 keV observed by THEMIS as well as the modeled IB for these two energies (black stars) for different Kp and P_{SW} levels. (The observed anisotropy for 1 keV ions is not compared because it has been shown to be strongly affected by field-aligned ionosphere outflow during disturbed time [*Wang et al.*, 2012].) The occurrence of isotropic distribution is high at larger r but drops sharply to very low in the inner magnetosphere. The sharp drops for 27.7 keV are located at smaller radial distances than those of 12.3 keV. The locations of the sharp drops match reasonably well with the modeled IBs for both energies at midnight and postmidnight MLTs, indicating that TCS scattering is likely the main isotropization mechanism. However, near dusk during higher Kp levels, occurrence is still high in the region earthward of the modeled IB. Simulations have shown that enhanced EMIC waves during a storm can result in pitch angle scattering predominantly in the inner magnetosphere

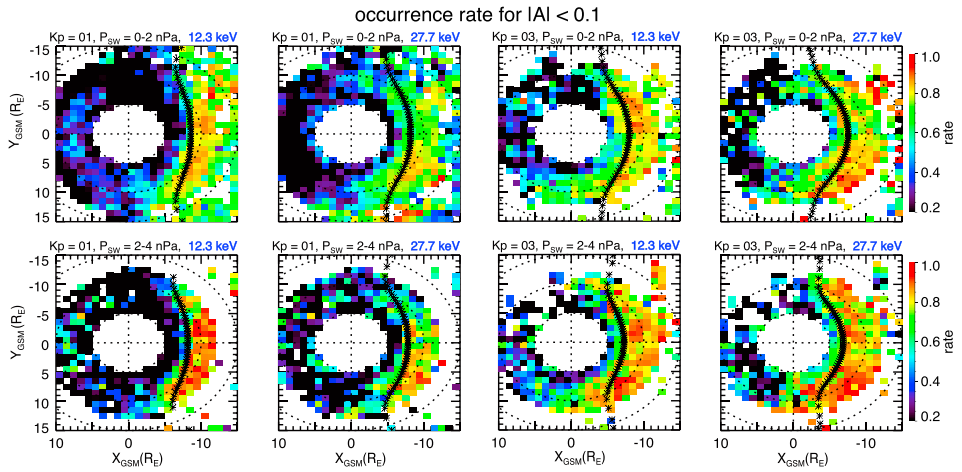

Figure 3. The occurrence rates for highly isotropic protons of 12.3 and 27.7 keV observed by THEMIS for different *Kp* and P_{SW} levels. The black stars mark the modeled IB for the two proton energies.

from the dusk to noon MLTs [*Jordanova et al.*, 2001]. THEMIS wave observations also show that EMIC waves are more frequently observed in that region [*Usanova et al.*, 2012]. Thus, isotropization due to higher wave power during higher *Kp* may account for this discrepancy near dusk.

3.2. Isotropic Boundary Latitudes

Strong pitch angle scattering by the TCS or waves results in filling of the loss cone. Thus, an IB should be a boundary separating distributions with or without filled loss cone. However, the loss cone at the equator is much smaller (~1° or so) than the pitch angle resolution of particle detectors, for example, 22° for the THEMIS detectors is far larger than the size of the equatorial loss cone. It is thus worthwhile to also examine observations from a low-altitude satellite, such as FAST, to determine the IB. Figure 4 illustrates three examples of IB observed by FAST. The top three rows show the ion energy fluxes above 1 keV as a function of latitude over three different pitch angle ranges. FAST was in the Northern Hemisphere in these three passes, so the particles at 0–30 pitch angle are within the downward loss cone, those at 60–150 pitch angle

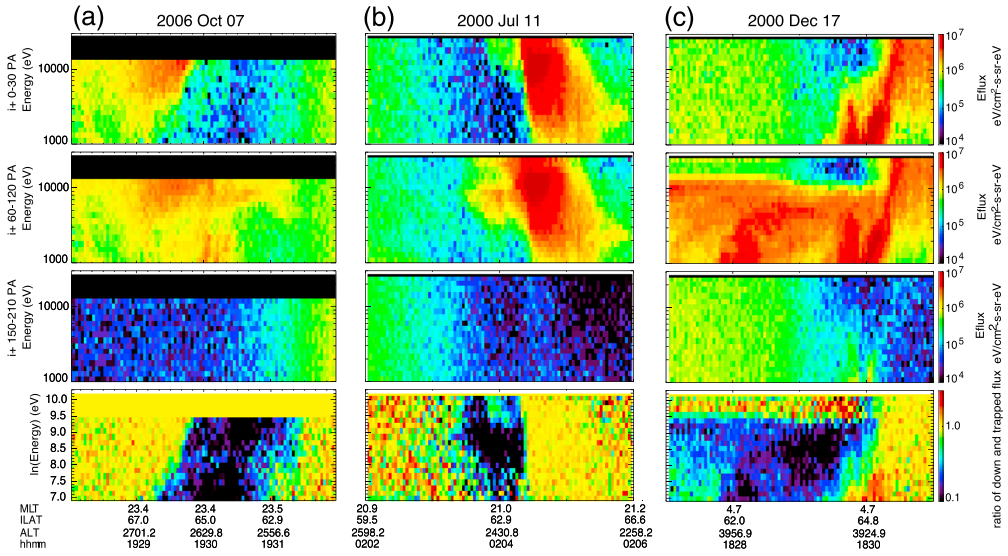

Figure 4. The ion energy fluxes measured by FAST within three different pitch angle ranges and the ratio of precipitating and trapped ion flux of ion from 1 to 30 keV ions (note that the *Y* axis for the ratio plots is ln(*E*) for showing better the energy dependence) for three events: (a) 7 October 2006, (b) 11 July 2000, and (c) 17 December 2000. The *X* axis shows magnetic local time (MLT), invariant latitude (ILAT), and the altitude (ALT) of FAST satellite and the universal time.

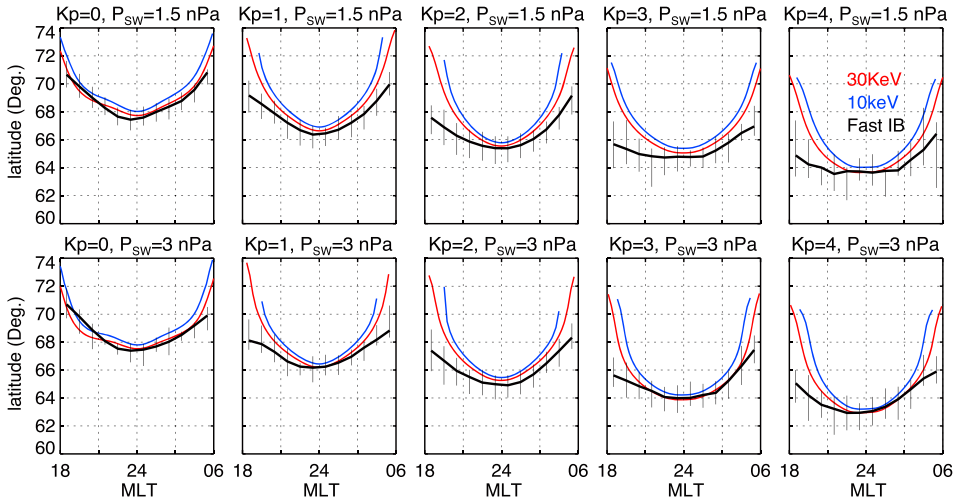

Figure 5. The IB invariant latitudes observed by FAST (the black curves indicate the median and the black vertical lines indicate the 25% and 75% quartiles) as a function of MLT for different *Kp* and P_{SW} levels. The modeled IB latitudes in the ionosphere for 10 (the blue lines) and 30 (the red lines) keV protons.

are trapped, and those at 150–210 pitch angle are within the upward loss cone going away from the ionosphere. The bottom row shows the ratio between the precipitating fluxes and the trapped fluxes, a ratio of 1 indicating a completely full loss cone. The IB can be identified as the boundary where the ratio drops sharply from 1.

In Figure 4a, the IB latitudes show strong energy dependence, decreasing approximately linearly with increasing ln(*E*), consistent with what would result from TCS scattering. However, sometimes the IB has almost no energy dependence as shown in Figure 4b. There are also limited cases with the IB latitude higher for higher-energy ions as illustrated in Figure 4c. This is likely due to scattering by EMIC waves, since EMIC waves are capable of scattering lower energy protons into loss cone more efficiently based on simulated pitch angle diffusion coefficients [*Liang et al.*, 2014]. Since the IBs caused by the TCS and by waves have opposite energy dependences, the IB shown in Figure 4b and many more cases with complex IB latitude distributions may result from a combination of both TCS and wave scattering.

Figure 5 shows statistical distributions of the IB latitudes observed by FAST as a function of MLT for different *Kp* and P_{SW} levels. These IB events are selected by examining the FAST pitch angle spectrograms of ion energy flux integrated from 1 keV to the highest available energy channel (approximately 20 keV), and the IB latitudes are determined as the location of a sharp transition from a near-isotropic distribution (except for an upgoing loss cone) to a near-empty downgoing loss cone occurs as illustrated in Figure 2 of *Donovan et al.* [2003b], and thus, the IBs here include all the different types of IB as discussed above regarding Figure 4. The FAST IB latitude is the lowest at midnight and moves to higher latitudes toward dawn/dusk. The IBs move to lower latitudes as *Kp* or P_{SW} increases. Also shown in Figure 5 are the modeled IBs of 10 (blue lines) and 30 keV (red lines) protons mapped to the ionosphere for different *Kp* and P_{SW}. It can be seen that the dependences of modeled IB latitudes on MLT, *Kp*, and P_{SW} are consistent with those of the FAST IBs, indicating TCS scattering is a major mechanism for the IB formation.

As shown in Figure 2, the modeled equatorial IB is closer to the Earth at midnight than at dawn and dusk due to tail magnetic field being more stretched at midnight. In addition, the equatorial IB maps to a lower latitude under more stretched field lines. Thus, the IB latitude is the lowest at midnight. Similarly, higher *Kp* or P_{SW} causes stronger cross-tail current and thus more stretched magnetic field lines, resulting in earthward motion of the equatorial IB and lower mapping latitudes of IB. The modeled IB matches fairly well with FAST IB for $Kp = 0$. As *Kp* becomes higher, the agreement at midnight remains generally good but discrepancy becomes larger at other MLTs, more so at the premidnight MLTs. The lager discrepancy near dusk is similar to that seen in the equatorial comparisons shown in Figure 3 and can be likely contributed by EMIC waves scattering.

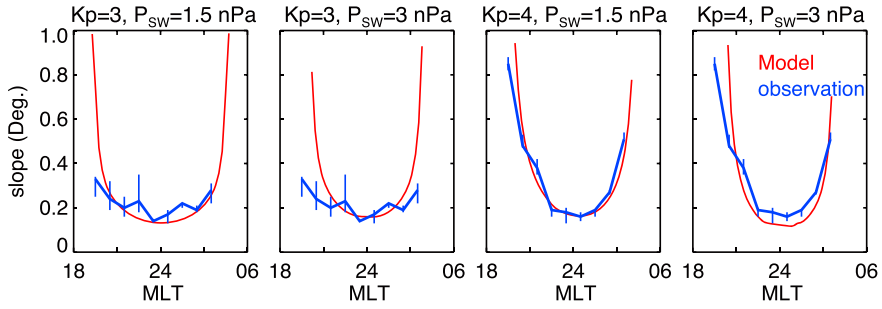

Figure 6. The slope comparison between the modeled (the red curves) and FAST IB (the blue curves) for $Kp = 3$ and 4 as a function of MLT. The FAST results are sorted only with *Kp*, so the two blue curves for different P_{SW} under the same *Kp* are identical.

3.3. Isotropic Boundary Due To Current Sheet Scattering

Our results indicate that current sheet scattering is generally the dominant mechanism for the IB formation except on the duskside during active times where we often see discrepancies. To further investigate if TCS scattering can account for the energy dependence of IBs during active times when the effects of other processes are minimized, we selected cases having the observed at higher latitudes for lower energy like the example shown in Figure 4a. We identified 339 FAST IB cases with IB showing clearly this kind of energy dependence for $Kp = 3$ (255 out of 2170 cases) and for $Kp = 4$ (84 out of 1034 cases). For high *Kp* cases, due to the increasing wave activity and disturbances such as tail flow bursts and substorms, the clear energy dependence cases as shown in Figure 4a are infrequent.

To quantify the energy dependence, we define a slope parameter, slope = (lat1–lat2)/(ln(*E*1)–ln(*E*2)); here we choose $E1 = 1$ keV and *E*2 is the highest energy measured by the ESA (which varied from 16 to 25 keV), and lat1 and lat2 are the IB latitudes corresponding to energies *E*1 and *E*2, respectively. We choose to use logarithm because the IB shows more clearly the linear dependence with logarithmic energy as illustrated in Figure 4a. Figure 6 shows the slope comparisons between our model (the red curves) and the observation (the blue curves) as a function of MLT for $Kp = 3$ and 4 (note that the observation result is only sorted with *Kp*). It can be seen that the modeled slopes match reasonably well with the FAST slopes. This further confirms the important role of TCS scattering in the IB formation but also implies that other processes can be important in addition when magnetic activity is high.

4. Discussion

4.1. Comparison of T89 Modeled IB With FAST Observations

As discussed in *Yue et al.* [2013], our force-balanced magnetic field configurations in the tail plasma sheet are characteristically different from those of the T89 field. Here we investigate the difference in the IB predictions between the T89 and our field. Figure 7 shows modeled IBs computed from the T89 fields for 10 and 30 keV protons under different *Kp* and their comparisons with the FAST IBs. Since the only control parameter for the T89 model is *Kp* index, we have binned the FAST IB observation to different *Kp* levels only (including all P_{SW} levels)

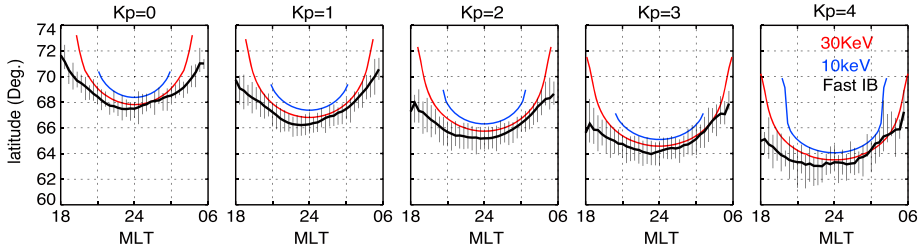

Figure 7. The MLT distribution of the IB latitudes for 10 (the blue lines) and 30 (the red lines) keV protons in the ionosphere computed from the T89 model in comparison with the FAST IB (the black curves) for different *Kp* levels.

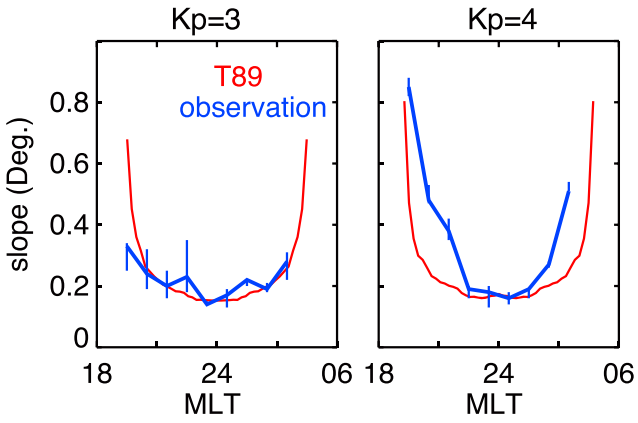

Figure 8. Comparison of the slopes between the IB computed from the T89 model (the red curves) and that from FAST observation (the blue curves) for $Kp = 3$ and 4 as a function of MLT.

in Figure 7. In general, the T89 IBs move to higher latitudes from midnight toward dawn/dusk, and they move to lower latitudes as energy increases, similar to the IBs computed from our force-balanced fields. In general, T89 IB latitudes are higher than the FAST IB latitudes for all *Kp* levels, and the discrepancy is larger at the premidnight than postmidnight MLTs for $Kp > 2$. Compared with our results shown in Figure 5, our IBs are closer to the observed IBs, particularly for high solar wind dynamic pressure and/or low *Kp* levels. In addition, the latitude difference between the 10 and 30 keV T89 IBs is ~0.8, about a factor of 2 larger than that in our IBs. Figure 8 shows the slope comparisons between the T89 and FAST IBs for $Kp = 3$ and 4. The T89 slope matches relatively well with the observations for $Kp = 3$ but less well for $Kp = 4$. On the other hand, our slopes shown in Figure 6 have good agreement with the observations for both $Kp = 3$ and 4. The above improvement in predicting the IBs achieved by our model indicates that taking into account the physical requirement of force balance leads to a more accurate description of the magnetic field configuration and also reinforces the confidence in our conclusions regarding the role of current sheet scattering for <30 keV ions.

4.2. Discrepancy Between Our Modeled IB and the Observations

As shown in section 3, our modeled IB displays some discrepancies with the THEMIS/FAST observation, especially around duskside during geomagnetic active times. In addition to the wave scattering mentioned previously, it can also be due to our model underestimating the ring current pressure and thus magnetic field stretching in the inner magnetosphere during more active time. For the empirical pressure model we established and used as the input for computing the force-balanced magnetic field, the pressure data inside $r = 8\ R_E$ are from the THEMIS measurements between 2007 and 2010, a period that closely surrounds the solar minimum. We compared the probability distributions of *Dst* and P_{SW} for the periods of 2007–2010 and 1997–2002 (the period for the majority of the FAST data used in the statistics shown in Figure 5). There is no clear difference in P_{SW} during different *Kp* levels. However, the difference in *Dst* is small when *Kp* is low but becomes larger with increasing *Kp*. For $Kp = 4$, the average (standard deviation) is −29 (±20) nT for 2007–2010 and −19 (±14) nT for 1997–2002. The relatively lower *Dst* during the THEMIS period indicates relatively lower ring current pressure and less stretched field lines, which likely contributed to the latitude discrepancy between our predicted IB and the FAST IB. Therefore, in the future, adjusting the model ring current pressure by a factor based on the *Dst* during the target period, as well as including more data in our empirical pressure model from THEMIS and other satellites during different phases of a solar cycle, should further improve the accuracy of our modeled magnetic field configuration.

In addition, the disagreement during geomagnetic active time may arise from other processes such as those related to tail flow bursts and substorm expansions. It is well known that flow bursts and substorms have a preference for the premidnight region, suggesting a dawn-dusk asymmetry scattering related to these disturbances.

5. Conclusion

In this study, we have investigated the role of tail current sheet scattering in the IB formation based on our 3-D force-balanced magnetic field model. We first computed the ion TCS scattering parameter on the equatorial plane and the ion IB mapped to the ionosphere for protons from 1 to 30 keV. Then we compared our model results with high-/low-altitude satellite observations by THEMIS/FAST. We have found that the dependences of modeled IB latitudes on MLT, energy, *Kp*, and P_{SW} are consistent with those of FAST IBs: the IB

moves to higher latitudes from midnight toward dawn/dusk and to lower latitudes as energy increases and as *Kp* or P_{SW} increases. The modeled IB at the equator is located around the inner boundary of the highly isotropic ion distribution observed by THEMIS at midnight and postmidnight, while there is larger discrepancy at premidnight under higher *Kp*. The modeled IB matches fairly well with FAST IB for $Kp = 0$.

As *Kp* becomes higher, the agreement at midnight remains generally good, but discrepancy becomes larger at dusk. Thus, our results indicate that while current sheet scattering is generally the dominant effect, other effects could be important on the duskside during active times. This duskside discrepancy can likely be accounted for by pitch angle scattering by EMIC waves, which is expected to be more effective at dusk to noon MLTs and during higher geomagnetic activity. For the FAST IB that has the energy dependence of lower latitude for higher energy, our model is capable of quantitatively producing the observed energy dependence. These model-observation comparisons strongly indicate that current sheet scattering plays a major role in the IB formation for the 1–30 keV main plasma sheet ion population, similar to the conclusions from the previous studies on >30 keV ions. Furthermore, the overall better agreement in the model comparison achieved by our force-balanced field than by the T89 indicates that taking into account the physical constraint of force balance in a model can provide more accurate description of the magnetic configuration and also reinforces our conclusions regarding the role of current sheet scattering for <30 keV ions.

Acknowledgments

The work by C. Yue, C.-P. Wang, and L.R. Lyons at UCLA has been supported by NASA grants NNX11AJ12G and NNX08A135G, NSF grant ATM-1003595, and IGPPS Program at Los Alamos National Laboratory. The work by S.G. Zaharia has been supported by NSF grants 1131873 and 1203460, NASA grant NNH10AP09I, and by the IGPPS Program at Los Alamos National Laboratory. The FAST data used in this study come exclusively from the publicly available ESA ion data provided by CDAWeb.

Michael Liehmon thanks Anita Cullen and one anonymous reviewer for their assistance in evaluating this paper.

References

Carlson, C. W., R. A. Pfaff, and J. G. Watzin (1998), The fast auroral snapshot (FAST) mission, *Geophys. Res. Lett.*, *25*(12), 2013–2016, doi:10.1029/98GL01592.

Donovan, E. F., B. J. Jackel, I. Voronkov, T. Sotirelis, F. Creutzberg, and N. A. Nicholson (2003a), Ground-based optical determination of the b2i boundary: A basis for an optical MT-index, *J. Geophys. Res.*, *108*(A3), 1115, doi:10.1029/2001JA009198.

Donovan, E. F., B. Jackel, R. Strangeway, and D. Klumpar (2003b), Energy dependence of the latitude of the 1–25 KeV ion isotropy boundary, *Sodankylä Geophys. Obs. Publ.*, *92*, 11–14.

Ganushkina, N. Y., T. I. Pulkkinen, M. V. Kubyshkina, V. A. Sergeev, E. A. Lvova, T. A. Yahnina, and T. Fritz (2005), Proton isotropy boundaries as measured on mid- and low-altitude satellites, *Ann. Geophys.*, *23*(5), 1839–1847.

Jordanova, V. K., C. J. Farrugia, R. M. Thorne, G. V. Khazanov, G. D. Reeves, and M. F. Thomsen (2001), Modeling ring current proton precipitation by electromagnetic ion cyclotron waves during the May 14–16, 1997, storm, *J. Geophys. Res.*, *106*(A1), 7–22, doi:10.1029/2000JA002008.

Liang, J., E. Donovan, B. Ni, C. Yue, F. Jiang, and V. Angelopoulos (2014), On an energy-latitude dispersion pattern of ion precipitation potentially associated with magnetospheric EMIC waves, *J. Geophys. Res. Space Physics*, *119*, doi:10.1002/2014JA020226, in press.

Lvova, E. A., V. A. Sergeev, and G. R. Bagautdinova (2005), Statistical study of the proton isotropy boundary, *Ann. Geophys.*, *23*(4), 1311–1316, doi:10.5194/angeo-23-1311-2005.

McCollough, J. P., J. L. Gannon, D. N. Baker, and M. Gehmeyr (2008), A statistical comparison of commonly used external magnetic field models, *Space Weather*, *6*, S10001, doi:10.1029/2008SW000391.

Newell, P. T., V. A. Sergeev, G. R. Bikkuzina, and S. Wing (1998), Characterizing the state of the magnetosphere: Testing the ion precipitation maxima latitude (b2i) and the ion isotropy boundary, *J. Geophys. Res.*, *103*(A3), 4739–4745, doi:10.1029/97JA03622.

Sergeev, V. A., and B. B. Gvozdevsky (1995), Mt-index: A possible new index to characterize the magnetic configuration of the magnetotail, *Ann. Geophys.*, *13*, 1093–1103, doi:10.1007/s00585-995-1093-9.

Sergeev, V. A., and M. V. Malkov (1988), Diagnostic of the magnetic configuration of the plasma sheet from measurements of energetic electrons above the ionosphere, *Geomagn. Aeron.*, *28*, 649–653.

Sergeev, V. A., and N. A. Tsyganenko (1982), Energetic particle losses and trapping boundaries as deduced from calculations with a realistic magnetic field model, *Planet. Space Sci.*, *10*, 999–1006.

Sergeev, V. A., E. M. Sazhina, N. A. Tsyganenko, J. A. Lunbland, and F. Soraas (1983), Pitch angle scattering of energetic protons in the magnetotail current sheet as the dominant source of their isotropic precipitation into the nightside ionosphere, *Planet. Space Sci.*, *31*, 1147–1158.

Sergeev, V. A., M. Malkov, and K. Mursula (1993), Testing the isotropic boundary algorithm method to evaluate the magnetic field configuration in the tail, *J. Geophys. Res.*, *98*(A5), 7609–7620, doi:10.1029/92JA02587.

Shevchenko, I. G., V. Sergeev, M. Kubyshkina, V. Angelopoulos, K. H. Glassmeier, and H. J. Singer (2010), Estimation of magnetosphere-ionosphere mapping accuracy using isotropy boundary and THEMIS observations, *J. Geophys. Res.*, *115*, A11206, doi:10.1029/2010JA015354.

Usanova, M. E., I. R. Mann, J. Bortnik, L. Shao, and V. Angelopoulos (2012), THEMIS observations of electromagnetic ion cyclotron wave occurrence: Dependence on AE, SYMH, and solar wind dynamic pressure, *J. Geophys. Res.*, *117*, A10218, doi:10.1029/2012JA018049.

Wang, C.-P., S. G. Zaharia, L. R. Lyons, and V. Angelopoulos (2012), Spatial distributions of ion pitch angle anisotropy in the near-Earth magnetosphere and tail plasma sheet, *J. Geophys. Res.*, *118*, 1–12, doi:10.1029/2012JA018275.

Wang, C.-P., S. Chao Yue, X. Zaharia, L. Xing, V. Lyons, T. N. Angelopoulos, and T. Lui (2013), Empirical modeling of plasma sheet pressure and three-dimensional force-balanced magnetospheric magnetic field structure: 1. Observation, *J. Geophys. Res. Space Physics*, *118*, 6154–6165, doi:10.1002/jgra.50585.

Yue, C., C.-P. Wang, S. G. Zaharia, X. Xing, and L. Lyons (2013), Empirical modeling of plasma sheet pressure and three-dimensional force-balanced magnetospheric magnetic field structure: 2. Modeling, *J. Geophys. Res. Space Physics*, *118*, 6166–6175, doi:10.1002/2013JA018943.